Measurement 158 (2020) 107710

Contents lists available at ScienceDirect

Measurement

journal homepage: www.elsevier.com/locate/measurement

Drift angle compensation method for a high-resolution and wide-range space camera

Wenyan Li [a,b,c], Chunhui Hu [a], Lei Zhang [a,c], Changxiang Yan [a,*]

[a] Changchun Institute of Optics, Fine Mechanics and Physics, Chinese Academy of Sciences, Changchun 130033, PR China
[b] University of Chinese Academy of Sciences, Beijing 100039, PR China
[c] Chang Guang Satellite Technology Co., Ltd, Changchun 130000, PR China

ARTICLE INFO

Article history:
Received 7 December 2019
Received in revised form 11 February 2020
Accepted 3 March 2020
Available online 14 March 2020

Keywords:
High-resolution
Wide-range
Space camera
Drift angle
Linearity

ABSTRACT

A high-resolution remote sensing satellite with a large ground swath width requires on-orbit compensation of the drift angle. However, there are large differences between drift angles of different positions on the focal plane. According to the research status, this paper proposes to compensate the average drift angle by satellite yaw angle adjustment, after which the focal plane adjustment mechanism in the camera can be used to eliminate the residual error. In this paper, drift angle calculation and the compensation method for a high-resolution, wide-range space camera were conducted. For further improvement of the compensation precision, a high linearity motion focal-plane adjustment mechanism was designed according to the drift angle. Theoretical calculation and nonlinear residual analysis of the mechanism motion were carried out and verified by laboratory tests. Test results showed high motion linearity of the mechanism and were in good agreement with the theoretical analysis results. Finally, MTF analysis was carried out and showed that the nonlinear error of the mechanism contributes little to MTF reduction and is small enough to be neglected. The MTF reduction decreases by 42.9% after mechanism further compensation of drift angle, and the result satisfies the imaging quality requirement of TDICCD.

1. Introduction

Time-delay-and-integration charge-coupled Devices (TDICCDs) are widely used in the push-broom mode in space cameras. The earth's rotation, orbital motion, satellite attitude change, and other factors will create a drift angle, that is, the angle between the push-broom direction and the target motion direction on the image plane. The drift angle produces a lateral image shift perpendicular to the push-broom direction, which results in modulation transfer function (MTF) drop and degrades the imaging quality [1–4].

In published literature, two methods usually work for average compensation of drift angle. One is to control satellites to adjust the yaw angles in order to make them approximately equal to the average drift angles [5,6]. The other is to rotate the focal plane by mechanisms in cameras [7–10], after which the line direction of TDICCD will be perpendicular to the overall image shifts.

The above two methods are only applicable to space cameras with narrow ranges, because they only adjust the focal plane as a whole to ensure the line direction of the focal plane center perpendicular to the image motion direction, the drift angle differences between positions on the focal plane are neglected. With the rapid development of space technology, demands for large-scale and high-speed target acquisition have become increasingly intense. Space cameras are being developed for high-resolution and wide-range directions. Wide-range cameras have large focal-plane sizes, resulting in large drift angle differences between positions on the focal planes. High resolution leads to small pixels, high TDICCD levels, and low tolerances for drift angles. Therefore, yaw angle adjustment or camera adjusting mechanisms alone to compensate for the average drift angle cannot meet the imaging requirement of high-resolution, wide-range cameras.

This paper proposes to compensate the average drift angle by yaw angle adjustment and eliminate the residual error by a focal plane adjustment mechanism in the camera. Firstly, drift angles at different positions on the focal plane will be obtained by theoretical calculation [11–20]. Then the focal plane will be divided into regions to distinguish between areas for averagely compensation by yaw angle adjustment or ones also for further compensation by mechanism according to the theoretical calculation result. So the residual error will be partially eliminated by the mechanism compensation according to the imaging requirement. Moreover, the motion nonlinearity and position error also influent

* Corresponding author.
E-mail addresses: liwenyan@charmingglobe.com (W. Li), zhanglei@charmingglobe.com (L. Zhang), liwy0130@126.com (C. Yan).

https://doi.org/10.1016/j.measurement.2020.107710
0263-2241/

the drift angle compensation result, so the high linearity of the focal-plane adjustment mechanism will be designed to minimize the imaging quality degrade cause of the motion nonlinearity.

2. Drift angle compensation analysis and adjustment mechanism design

2.1. Drift angle calculation

For purpose of obtaining the drift angles at different positions on the focal plane, image motion calculation was conducted. By coordinate transformations, the relationship between the earth objects and images on the focal plane was found and the image motion velocity vector equation was derived. The established coordinates mainly include: Geocentric inertial coordinate I(I_1, I_2, I_3), Geodetic coordinate E(E_1, E_2, E_3), Spacecraft orbital coordinate B(B_1, B_2, B_3), Geographical coordinate G(G_1, G_2, G_3), Spacecraft coordinate S(S_1, S_2, S_3), SORS coordinate C(C_1, C_2, C_3) and Image plane coordinate P(P_1, P_2, P_3). The detailed coordinate transformation operations are given as Fig. 1. The equation for transformation from coordinate G to P is given in Eq. (1).

$$
\begin{aligned}
P = \begin{bmatrix} P_1 \\ P_2 \\ P_3 \\ 1 \end{bmatrix} = {} & \begin{bmatrix} -\frac{f}{(H-h)} & 0 & 0 & 0 \\ 0 & \frac{f}{(H-h)} & 0 & 0 \\ 0 & 0 & \frac{f}{(H-h)} & -f \\ 0 & 0 & 0 & 1 \end{bmatrix} \begin{bmatrix} \cos\psi_0 & \sin\psi_0 & 0 & 0 \\ -\sin\psi_0 & \cos\psi_0 & 0 & 0 \\ 0 & 0 & 1 & 0 \\ 0 & 0 & 0 & 1 \end{bmatrix} \\
& \begin{bmatrix} \cos\theta_0 & 0 & -\sin\theta_0 & 0 \\ 0 & 1 & 0 & 0 \\ \sin\theta_0 & 0 & \cos\theta_0 & 0 \\ 0 & 0 & 0 & 1 \end{bmatrix} \begin{bmatrix} 1 & 0 & 0 & 0 \\ 0 & \cos\varphi_0 & \sin\varphi_0 & 0 \\ 0 & -\sin\varphi_0 & \cos\varphi_0 & 0 \\ 0 & 0 & 0 & 1 \end{bmatrix} \begin{bmatrix} 1 & 0 & 0 & 0 \\ 0 & 1 & 0 & 0 \\ 0 & 0 & 1 & -(R+H) \\ 0 & 0 & 0 & 1 \end{bmatrix} \\
& \begin{bmatrix} \cos(\gamma_0+\Omega t) & 0 & \sin(\gamma_0+\Omega t) & 0 \\ 0 & 1 & 0 & 0 \\ -\sin(\gamma_0+\Omega t) & 0 & \cos(\gamma_0+\Omega t) & 0 \\ 0 & 0 & 0 & 1 \end{bmatrix} \begin{bmatrix} \cos i_0 & \sin i_0 & 0 & 0 \\ -\sin i_0 & \cos i_0 & 0 & 0 \\ 0 & 0 & 1 & 0 \\ 0 & 0 & 0 & 1 \end{bmatrix} \begin{bmatrix} \cos\omega t & 0 & \sin\omega t & 0 \\ 0 & 1 & 0 & 0 \\ -\sin\omega t & 0 & \cos\omega t & 0 \\ 0 & 0 & 0 & 1 \end{bmatrix} \\
& \begin{bmatrix} \cos i_0 & -\sin i_0 & 0 & 0 \\ \sin i_0 & \cos i_0 & 0 & 0 \\ 0 & 0 & 1 & 0 \\ 0 & 0 & 0 & 1 \end{bmatrix} \begin{bmatrix} \cos(\gamma_0) & 0 & -\sin(\gamma_0) & 0 \\ 0 & 1 & 0 & 0 \\ \sin(\gamma_0) & 0 & \cos(\gamma_0) & 0 \\ 0 & 0 & 0 & 1 \end{bmatrix} \begin{bmatrix} 1 & 0 & 0 & 0 \\ 0 & 1 & 0 & 0 \\ 0 & 0 & 1 & R \\ 0 & 0 & 0 & 1 \end{bmatrix} \begin{bmatrix} G_1 \\ G_2 \\ G_3 \\ 1 \end{bmatrix}
\end{aligned}
\tag{1}
$$

So the coordinates of a point P(P_1, P_2, P_3) are functions of time t and expressed as Eq. (2)

$$
P(t) = \begin{bmatrix} P_1 \\ P_2 \\ P_3 \\ 1 \end{bmatrix} = \begin{bmatrix} P_1(t) \\ P_2(t) \\ P_3(t) \\ 1 \end{bmatrix} \tag{2}
$$

$$
G \xrightarrow[\substack{Rotate(G_2):i_0}]{\substack{Shift(G_3):-R \\ Rotate(G_2):\gamma_0}} E \xrightarrow{Rotate(E_2):-\omega t} I \xrightarrow[\substack{Rotate(I_2):-(\gamma_0+\Omega t) \\ Shift(I_3):R+H}]{Rotate(I_3):-i_0} \qquad
B \xrightarrow[Rotate(B_3):\psi_0+\dot{\psi}t]{\substack{Rotate(B_1):\varphi_0+\dot{\varphi}t \\ Rotate(B_2):\theta_0+\dot{\theta}t}} S \xrightarrow{Scale:f/(H-h)} C \xrightarrow{Shift(C_3):f} P
$$

Fig. 1. Coordinate transformation operations for drift angle calculation.

By differential of P (t) with t and set t = 0, the image motion equation were obtained as Eq. (3)

$$
V_P = \left.\frac{dP}{dt}\right|_{t=0} = \begin{bmatrix} dP_1/dt \\ dP_2/dt \\ dP_3/dt \\ 0 \end{bmatrix} = \begin{bmatrix} V_{P1} \\ V_{P2} \\ V_{P3} \\ 0 \end{bmatrix} \tag{3}
$$

And the drift angle β of the point P was obtained as Eq. (4)

$$
\beta = \arctan\left(\frac{V_{P1}}{V_{P2}}\right) \tag{4}
$$

In Eqs. (1)–(4), the parameters were defined as follows.

R: Earth radius relative to geocentric (km).
H: Satellite orbital height measured from the object (km).
h: Object height (km).
i_0: Orbit obliquity (the angle between orbital plane and earth equator plane).
ω: Earth rotation angular speed.
Ω: Satellite orbital angular speed relative to geocentric.
γ_0: The central angle between the satellite and the ascending node in the orbital plane during imaging.
f: The focal length of the camera.
φ_0, θ_0, ψ_0: Yaw, pitch, and roll angle of S coordinate relative to G coordinate during imaging.

Substituting the specific parameters of the satellite shown in Table 1, the drift angle of different positions on the focal plane were obtained through calculation.

The optical field of view is 16.38°×0.7°, so the size of the focal plane reaches 1395.45 mm × 59.26 mm. The diagrammatic sketch of the focal plane is shown in Fig. 2. Thirty-three feature points equally divided the focal plane into twenty regions and O is the geometric center of focal plane. The drift angles of the feature points in different situations were calculated. The calculation results are shown in Fig. 3 and Fig. 4. It can be seen that when the satellite moves to the orbit central angle of 0° and the roll angle

Table 1
Parameters of the satellite for the drift angle calculation.

Item	1	2	3	4	5	6	7	8	9	10
Parameters	i_0 (°)	F (mm)	H (km)	h (km)	ψ_0 (°)	φ_0 (°)	θ_0 (°)	R (km)	Ω (s^{-1})	ω (s^{-1})
Values	97.53	4850	531	0	−45 to 45	0	0	6371	1.1×10^{-3}	7.292×10^{-5}

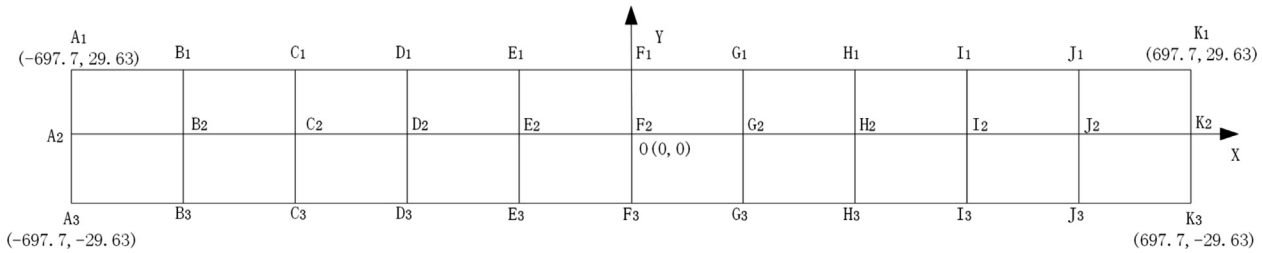

Fig. 2. Diagrammatic sketch of the focal plane.

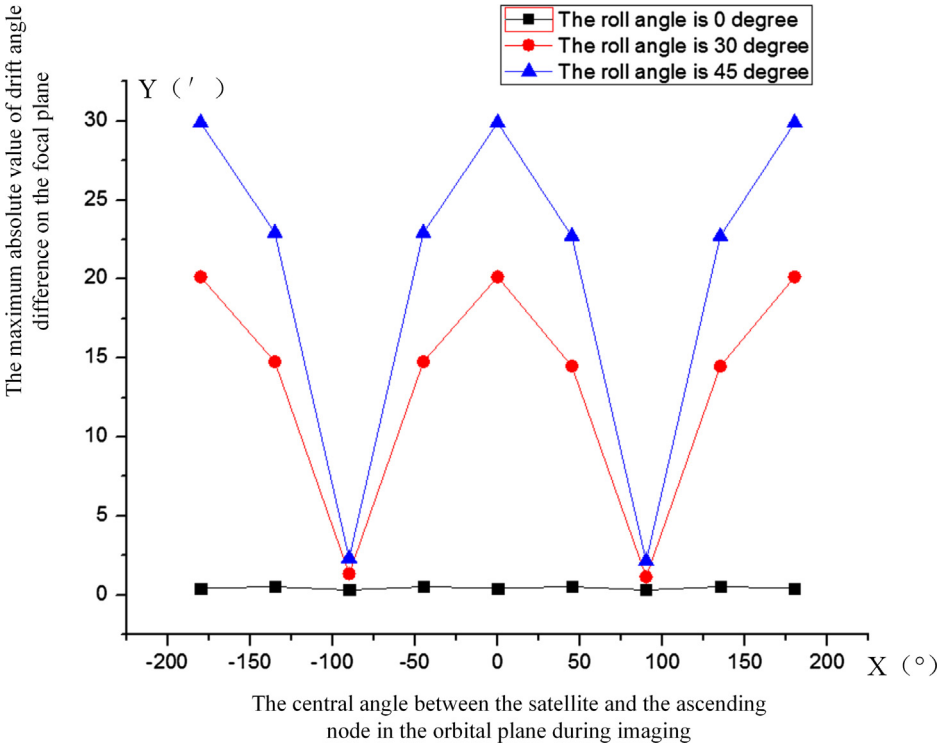

Fig. 3. The maximum absolute value of drift angle difference on the focal plane.

is 45°, the difference of the drift angles between positions of the focal plane reaches a maximum of 29.9′. The drift angle distribution under condition that the roll angle is 45° and the central angle is 0°is shown in Table 2.

We can see that in Table 2 the maximum and minimum drift angle is −172′ and −112.2′, and the average of the two is −142.1′, which is −2.37°. So the drift angle can be averagely eliminated by yaw angle adjustment of −2.37° and the drift angle distribution after average elimination is shown in Table 3. We can see that the maximum absolute value of drift angle was reduced to 29.9′ by yaw angle adjustment.

For further reduction of drift angle to meet the requirement of image quality, the angle of focal plane regions could be adjusted by camera mechanisms. For example, we can see in Table 3 that the maximum and minimum drift angle of $A_1A_3C_3C_1$ region is −29.9′ and −16.9′, and the average of the two is −23.4′. The maximum and minimum drift angle of $I_1I_3K_3K_1$ region is 29.9′ and 13.4′, and the average of the two is 21.7′. So the drift angle of $A_1A_3C_3C_1$ and $I_1I_3K_3K_1$ regions can be compensated by 23.4′ and 21.7′. The drift angle distribution after compensation is shown in Table 4, the maximum absolute value of drift angle was reduced to 19.5′. So it is 10.4′ which is effectively compensated.

2.2. Yaw angle adjustment of the satellite

We can see through the calculation and analysis result in Section 2.1 that in condition of different orbit position and roll angle, the drift angles on the focal plane distribute differently. We propose to conduct a average elimination by yaw adjustment according to the calculation result and then adjust the mechanisms in the camera to rotate the angle of some regions for further compensation. To conduct, we embedded the drift angle calculation method

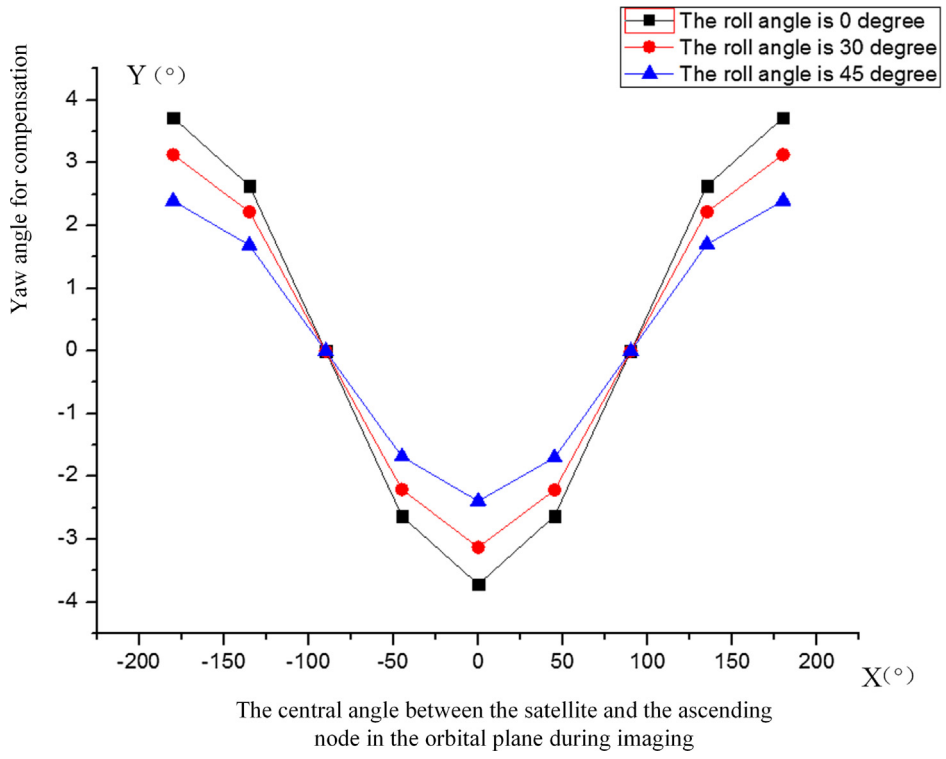

Fig. 4. The yaw angle for compensation.

Table 2
Drift angle distribution before average elimination by yaw angle adjustment.

Drift angle/(′)												
		Feature points										
		A	B	C	D	E	F	G	H	I	J	K
Item	1	−169.7	−164.4	−159.0	−153.6	−148.1	−142.5	−136.8	−130.9	−124.9	−118.6	−112.2
	2	−170.9	−165.6	−160.3	−155.0	−149.6	−144.6	−138.4	−132.7	−126.8	−120.7	−114.4
	3	−172.0	−166.8	−161.6	−156.4	−151.0	−145.6	−140.1	−134.5	−128.7	−122.8	−116.6

Table 3
Drift angle distribution after average elimination by yaw angle adjustment of −2.37°.

Drift angle/(′)												
		Feature points										
		A	B	C	D	E	F	G	H	I	J	K
Item	1	−27.6	−22.3	−16.9	−11.5	−6	−0.4	5.3	11.2	17.2	23.5	29.9
	2	−28.8	−23.5	−18.2	−12.9	−7.5	−2.5	3.7	9.4	15.3	21.4	27.7
	3	−29.9	−24.7	−19.5	−14.3	−8.9	−3.5	2	7.6	13.4	19.3	25.5

Table 4
Drift angle distribution after mechanism adjustment of both sides.

Drift angle/(′)												
		Feature points										
		A	B	C	D	E	F	G	H	I	J	K
Item	1	−4.2	1.1	−16.9	−11.5	−6	−0.4	5.3	11.2	17.2	1.8	8.2
	2	−5.4	−0.1	−18.2	−12.9	−7.5	−2.5	3.7	9.4	15.3	−0.3	6
	3	−6.5	−1.3	−19.5	−14.3	−8.9	−3.5	2	7.6	13.4	−2.4	3.8

into the satellite attitude control software, for control of different angle compensations and methods according to satellite's orbit positions and roll angles.

In the process of yaw angle adjustment, the satellite attitude control system works in the zero momentum mode with reaction flywheels as the actuators. The system mainly includes attitude controllers, actuators and attitude sensors, which provide satellite three-axis attitude information. In attitude adjustment, the current attitude quaternion $\boldsymbol{q}$ of the satellite are determined by the joint estimation of star sensors and gyroscopes, and the current angular

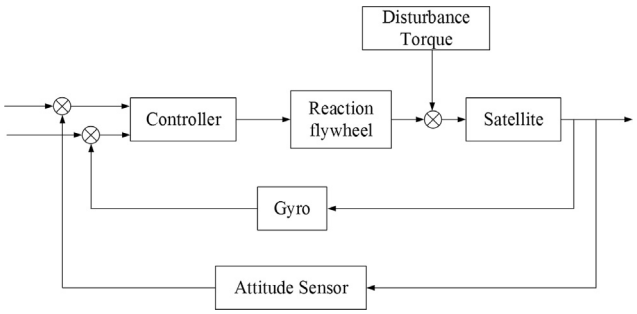

Fig. 5. The control system for yaw angle adjustment.

velocity $\boldsymbol{\omega}$ of the satellite are determined by the gyroscopes. The quaternion $\boldsymbol{q_d}$ of the target attitude and the desired angular velocity $\boldsymbol{\omega_d}$ can be obtained from the calculation results of the desired attitude and the yaw angle. The maneuvering quaternion and deviation angular velocity corresponding to the transition from the current attitude to the target attitude are $\boldsymbol{q_d}$ and $\boldsymbol{\omega_e}$. According to the quaternion multiplication, we can get Eq. (5).

$$q_e = q^{-1} \otimes q_d \tag{5}$$

The deviation angular velocity is shown as Eq. (6)

$$\omega_e = \omega_d - \omega \tag{6}$$

Then the desired control moment of satellite three axes can be obtained as Eq. (7)

$$T_u = -Kq_e - C\omega_e + \omega^* J\omega \tag{7}$$

Among them, K and C are proportional and differential coefficients, $\boldsymbol{\omega}^*$ is the cross-product matrix and J is inertia matrix of the satellite.

A reaction flywheel is installed on the three main inertia axes of the satellite. According to the above control algorithms, the control moments can be obtained, and then the attitude adjustment completed. The schematic diagram of the control system is shown in Fig. 5.

2.3. Design of the adjustment mechanism

Considering the advantage of a wide field of view and no central illusion, a three-mirror anastigmatic (TMA) system is broadly adopted in high-resolution, wide-range remote sensing cameras. The TMA system proposed in this paper met the technical requirement of a focal length of 4850 mm, swath of 150 km, and field of view of 16.38° × 0.7° on an orbit of 531 km. There are four mirrors in the optical system: the primary mirror M1, secondary mirror M2, tertiary mirror M3, and folding flat mirror M4, which reflect light onto the TDICCD focal plane. The schematic design of the optical system and optical ray trace layout for the optical system are shown in Fig. 6. The optical system is designed to be a quasi-far core optical path, which makes the projection distortion produced in the focal depth range when the image plane is out of focus. The advantage of TMA optical system for this space TDICCD camera was shown in this paper. In order to make the optical system structure more compact and have good structural stability, the flat mirror M4 is added between the TDICCD focal plane and the tertiary mirror M3, which plays an important role in folding optical path.

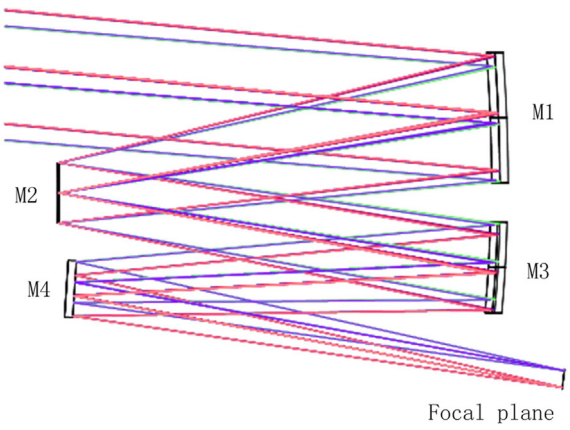

Fig. 6. Schematic design of the optical system and optical ray trace layout.

A long focal plane consisting of multiple TDICCDs is required for wide-range remote sensing cameras, and the method of TDICCD mechanical interleaving assembly is widely used. As the imaging field of view of the camera is 16.38° × 0.7°, the length of the focal plane reaches 1395.45 mm, which is much longer than the length of a single TDICCD. In this work, 50 TDICCDs (each TDICCD has 3248 pixels and the stages of the TDICCDs is 32) were assembled to make a long TDICCD focal plane. Accordingly, the total pixel number reached 162,400.

According to the drift angle calculation result introduced in Section 2.1 and the image quality requirement, we can provide a mechanism compensation strategy, according to which the focal plane would be divided into different regions and driven to rotate separately. Consider of the parameters which were used for calculation and given in Table 1 may have errors, and these errors will further affect the accuracy of the calculation results, the focal plane could be divided into five groups, which could be respectively controlled by a single mechanism, the principle of the mechanical interleaving assembly TDICCD focal plane is shown in Fig. 7. The schematic of the focal plane adjustment mechanism is shown in Fig. 8.

The middle three groups only compensate for defocusing. The two groups on both sides were drive to adjust the focal plane to compensate for the defocusing and drift angle, respectively. Both motions are driven by a stepper motor and use a worm gear for power transmission, deceleration, and self-locking. Power is transmitted to the screw nut pairs and the rotation of the screws is converted into the linear movement of the nuts. In the drift-angle compensation mechanism, the slider in the fork is mounted on the nut, which drives the fork fixed on the focal plane to achieve the focal plane rotation. In the defocusing mechanisms, the nuts are directly mounted on the focal plane substrates and achieve linear motion. Moreover, photoelectric angle encoders are mounted on the mechanisms to display the displacements and angles of the TDICCD focal planes. So we can see that the drift angle would be compensated by the two mechanism on both sides. In this way the residual drift angle will meet the demand of camera imaging, and it will be demonstrated in chapter 5.

3. Linear analysis of motion

This paper establishes a mathematical model for the drift-angle compensation motion, the schematic model of which is shown in Fig. 9. The drive component drives the screw so that it rotates, which in turn drives the nut so that it moves in a straight line. The slider is mounted on the nut and also moves in a straight line and drives the fork to move. The fork is fixedly connected to the moving block of the circular arc guide way, thereby driving the focal plane to rotate around the rotation axis.

The mathematical model of the drift-angle compensation motion is shown in Fig. 10. In the Cartesian coordinate system

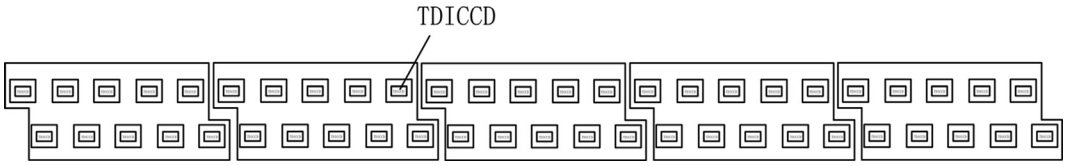

Fig. 7. Principle of mechanical interleaving assembly TDICCD focal plane.

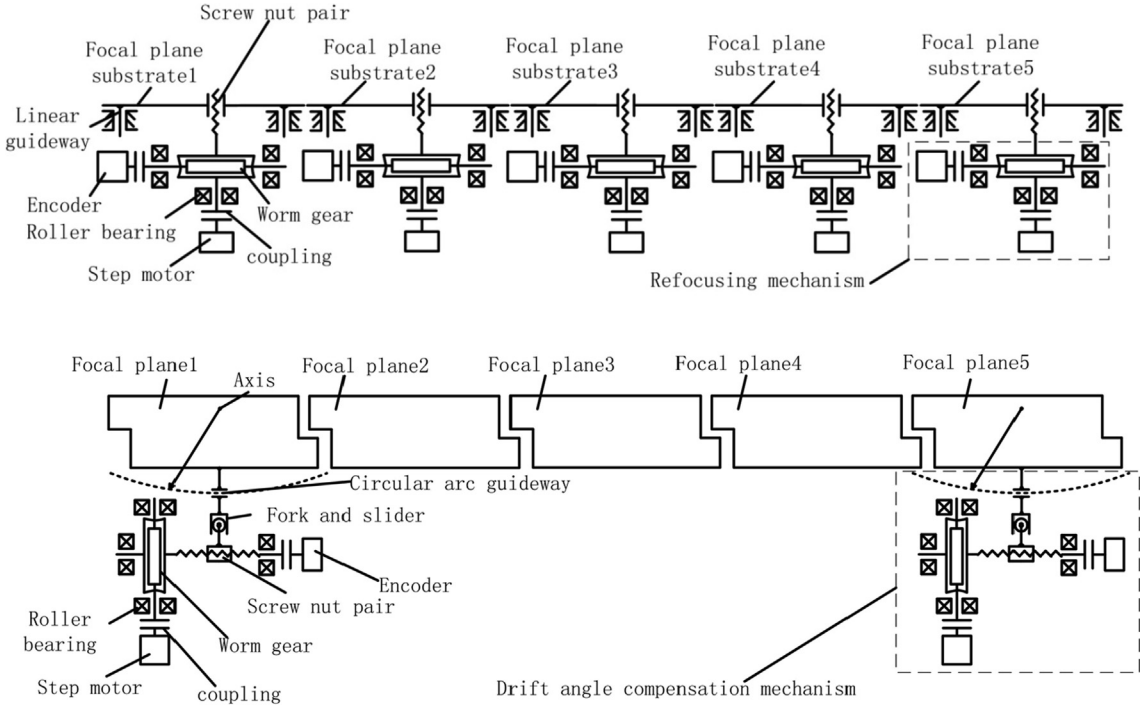

Fig. 8. Schematic of the focal plane adjustment mechanism.

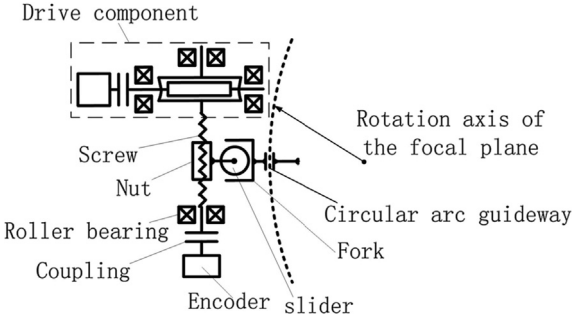

Fig. 9. Schematic model of the drift-angle compensation mechanism.

XOY, the straight line l_1 represents the axis where the nut moves along the screw, i.e., the screw axis; The point O represents the rotation axis of the focal plane; A_0B_0 is the position of the fork when the drift angle compensation magnitude α is 0°, D_0 represents the installation error. A_1B_1 is the position of the fork after the adjustment magnitude is α. Then K_0K_1 is the displacement of the slider.

Therefore, the expression for line l_1 is:

$$x = -L$$

The coordinates of point K_0 are:

$$\begin{bmatrix} -L \\ -D_0 \end{bmatrix}$$

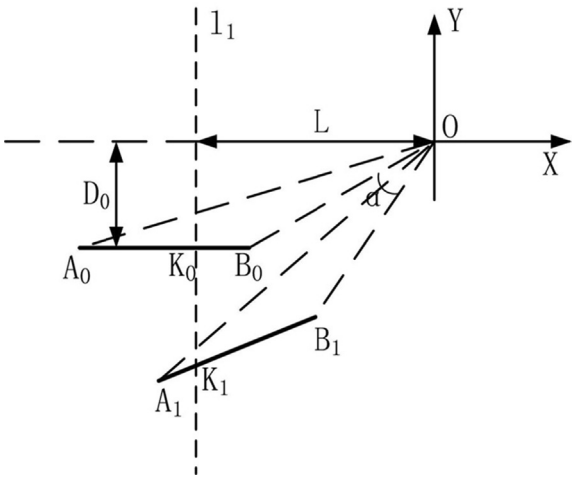

Fig. 10. Mathematical model of the drift-angle compensation mechanism.

The expression for line A_0B_0 is:

$$\rho = \begin{bmatrix} -L \\ -D_0 \end{bmatrix}, \vec{\eta} = \{1, 0\}$$

After rotating through an angle α around the Z-axis according to the right hand rule, line A_0B_0 reaches line A_1B_1, which represents the position of the fork after the adjustment magnitude is α. The equation for A_1B_1 is:

$$\rho_1 = \begin{bmatrix} \cos(-\alpha) & \sin(-\alpha) \\ -\sin(-\alpha) & \cos(-\alpha) \end{bmatrix} \begin{bmatrix} -L \\ -D_0 \end{bmatrix} = \begin{bmatrix} L\cos\alpha + D_0\sin\alpha \\ -L\sin\alpha - D_0\cos\alpha \end{bmatrix}$$

$$n_1 = \begin{bmatrix} \cos(-\alpha) & \sin(-\alpha) \\ -\sin(-\alpha) & \cos(-\alpha) \end{bmatrix} \begin{bmatrix} 1 \\ 0 \end{bmatrix} = \begin{bmatrix} \cos\alpha \\ \sin\alpha \end{bmatrix}$$

K_1 is the intersection of l_1 and A_1B_1, and its coordinates can be calculated as follows:

$$\rho_1 + x_1 \cdot \vec{n}_1 \in l_1$$

$$-L\cos\alpha + D_0\sin\alpha + x_1\cos\alpha = -L$$

$$x_1 = -L\frac{1-\cos\alpha}{\cos\alpha} - D_0\tan\alpha$$

The Y coordinate of point K_1 is:

$$-L\sin\alpha - D_0\cos\alpha - L(1-\cos\alpha)\tan\alpha - D_0\frac{\sin^2\alpha}{\cos\alpha}$$

The relationship between the drift-angle compensation magnitude and the movement magnitude of the slider is as follows:

$$|K_0K_1| = L\sin\alpha + L(1-\cos\alpha)\tan\alpha - D_0\left(1 - \frac{1}{\cos\alpha}\right) \quad (8)$$

The error analysis of Eq. (8) is carried out by Taylor series expansion, and Eq. (9) is obtained after the expansion.

$$|K_0K_1| = \frac{2L\alpha^5}{15} + \frac{5D_0\alpha^4}{24} + \frac{L\alpha^3}{3} + \frac{D_0\alpha^2}{2} + L\alpha \quad (9)$$

The angle adjustment range of the drift-angle compensation mechanism is 2°. L, which represents the distance between the rotation center of the focal plane and the axis of the screw, equal to 188.5 mm. The estimated value of D_0 is 1 mm, so the Eq. (9) is

$$|K_0K_1| = 25.1\alpha^5 + 0.2\alpha^4 + 62.8\alpha^3 + 0.5\alpha^2 + 188.5\alpha \quad (10)$$

after replacing α with 2° in Eq. (10), the contributions of each order item of Eq. (10) to the slider movement $|K_0K_1|$ were obtained, as shown in the second line of Table 5. After further deduction as follow.

$$\beta_i = \frac{s_i \cdot 2}{\sum_{i=1}^{5} s_i}$$

The contributions of each order item to the compensation angle were obtained, as given in the third line of Table 5. It can be seen that the sum of the contributions of the second item and the higher order items to the slider movement is 0.0033 mm, and that to the compensation angle is 0.06′.

4. Linear test of the mechanism

4.1. Test result

The design results of the focal plane compensation mechanism are shown in Fig. 11 and the linearity of the drift-angle compensation motion is tested, as shown in Fig. 12.

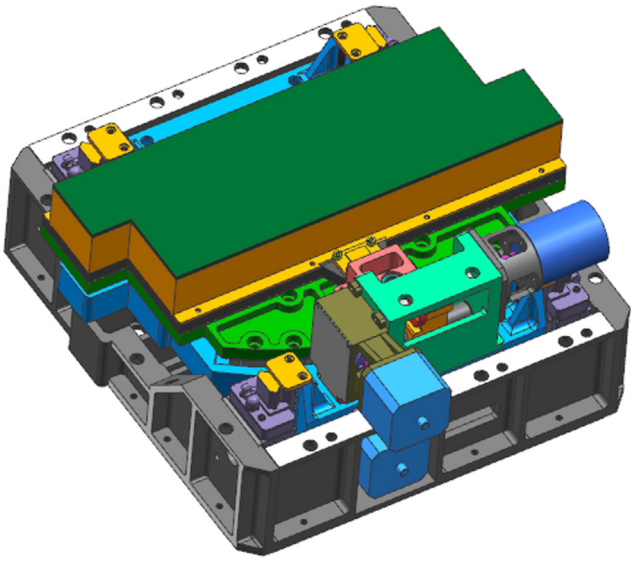

Fig. 11. Design results of the focal plane adjustment system.

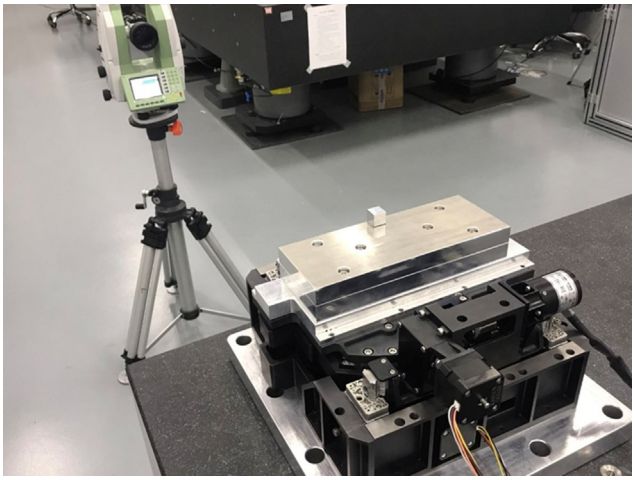

Fig. 12. Linearity test of the drift-angle compensation motion.

In the test, a stepper motor drive the motion and was controlled to rotate, and the power was transmitted to the screw nut pairs. Rotation of the screw was converted into the linear movement of the nut, which drive the fork fixed on the focal plane to achieve the focal plane rotation. A 16-bit photoelectric angle encoder was mounted on the other side of the screw, which recorded the rotation angle changes. Accordingly, the displacement of the slider in the fork could be calculated. The fork drive the focal plane to rotate around the rotation axis. A fine prism was adhered to the surface of the focal plane substitute, and a theodolite was fixed on the ground after leveling. So the angle changes of the prism were observed through the theodolite, which displayed the rotation angle of the focal plane. The schematic diagram of the test is shown in Fig. 13 and the test process in Fig. 14.

Table 5
Comparison of contributions of different order terms to the compensation angle.

Content	Parameters	Order				
		1	2	3	4	5
Contribution to slider movement/mm	s	6.58	0.00061	0.0027	3.09×10^{-7}	0.000021
Contribution to the compensation angle/′	β	119.9	0.011	0.049	5.64×10^{-6}	0.00038

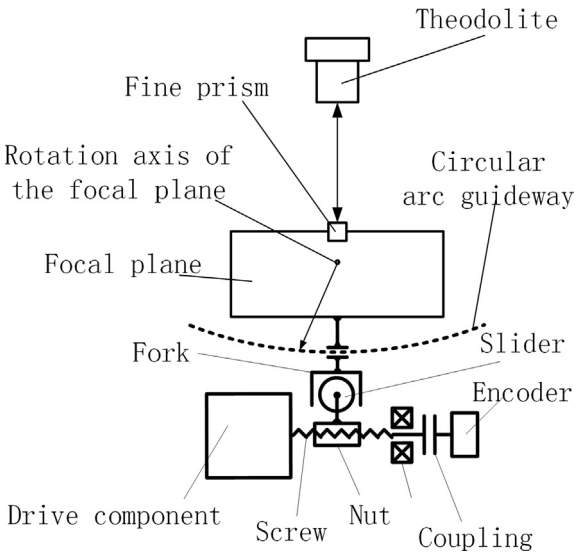

Fig. 13. Schematic diagram of the mechanism linearity test.

The test result is given in Table 6. In the table, Z is the angle code value of the encoder, K is the angle of the TDICCD focal plane, N is the angular value of K after conversion to radians, △N is the changing angle value of N. The pitch of the screw is 1.5 mm and the encoder number of digits is16-bit, so the displacements value of the nut were calculated by Eq. (11), which expressed in M,

$$M_{\mathrm{i}} = \frac{Z_i \cdot 1.5}{2^{16}} \tag{11}$$

△M is the changing displacement value of M;

4.2. Data analysis

As were introduced above, Z is the rotation angle of the screw, which was directly measured by the encoder. M represents the displacement of the nut converted from Z and N represents the rotation angle of the focal plane. In order to verify the theoretical analysis, M and N were linearly fitted to Eq. (12) by least squares fitting method. The primary term coefficient and non-primary residuals were compared with theoretical analysis result.

$$M = a \cdot \mathrm{N} + \mathrm{b} \tag{12}$$

According to the least-squares fitting method, the error between M_i *and* $a{\cdot}N + b$ *is* d_i, which is expressed as Eq. (13).

$$d_i = y_i - a - bx_i \tag{13}$$

Aiming at minimize the sum of d_i^2

$$D = \sum_{i=1}^{21} d_i^2 = \sum_{i=1}^{n} [y_i - a - b_i]^2$$

After finding first-order partial derivatives of D to a and b and making them equal to zero, we have

$$a = \frac{\overline{NM} - \overline{NM}}{\overline{N^2} - \overline{N}^2} \tag{14}$$

$$b = \overline{M} - a\overline{N} \tag{15}$$

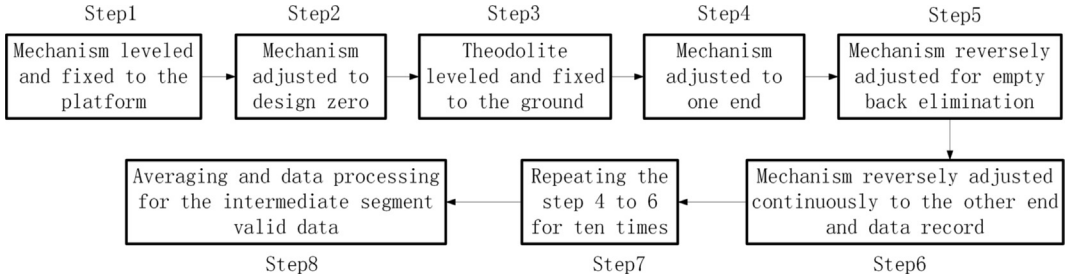

Fig. 14. Process of the mechanism linearity test.

Table 6
Test data of drift-angle compensation motion.

i	Z_i	M_i(mm)	$\triangle M_i$(mm)	K_i(°)	N_i	$\triangle N_i$
1	802,264	18.3624		2.0011	0.0349	
2	774,145	17.7188	0.6436	1.8037	0.0315	0.1974
3	746,015	17.0749	0.6439	1.5955	0.0278	0.2082
4	717,889	16.4312	0.6437	1.4017	0.0245	0.1938
5	689,765	15.7875	0.6437	1.2006	0.021	0.2011
6	661,666	15.1443	0.6432	0.9974	0.0174	0.2032
7	633,519	14.5001	0.6442	0.7991	0.0139	0.1983
8	605,420	13.857	0.6431	0.6007	0.0105	0.1984
9	577,263	13.2125	0.6445	0.4072	0.0071	0.1935
10	549,140	12.5688	0.6437	0.2055	0.0036	0.2017
11	521,000	11.9247	0.6441	−0.0027	0	0.2082
12	492,878	11.2811	0.6436	−0.1939	−0.003	0.1912
13	464,726	10.6367	0.6444	−0.3985	−0.007	0.2046
14	436,547	9.9918	0.6449	−0.6001	−0.011	0.2016
15	408,419	9.348	0.6438	−0.7986	−0.014	0.1985
16	380,249	8.7032	0.6448	−1.0004	−0.018	0.2018
17	352,114	8.0592	0.644	−1.2002	−0.021	0.1998
18	323,966	7.415	0.6442	−1.3970	−0.024	0.1968
19	295,800	6.7703	0.6447	−1.5972	−0.028	0.2002
20	267,659	6.1262	0.6441	−1.7972	−0.031	0.2000
21	239,470	5.481	0.6452	−1.9987	−0.035	0.2015

Table 7
Comparison between the fitting results and the theoretical calculation results.

Item	result	First-order coefficient *a*	Nonlinear Residual SSE (mm)
1	Theoretical calculation result	188.5	0.0033
2	Test result	184.6	0.0016

The correlation coefficient r is:

$$r = \frac{\overline{NM} - \overline{N}\,\overline{M}}{\sqrt{\left(\overline{N^2} - \overline{N}^2\right) - \left(\overline{M^2} - \overline{M}^2\right)}} \tag{16}$$

In Eqs. (14)–(16), the average values of the data elements are

$$\bar{M} = \frac{1}{21}\sum_{i=1}^{21} M_i = 11.9236$$

$$\bar{N} = \frac{1}{21}\sum_{i=1}^{21} N_i = 1.9 \times 10^{-5}$$

$$\overline{N^2} = \frac{1}{21}\sum_{i=1}^{21} N_i^{\,2} = 4.47 \times 10^{-4}$$

$$\overline{NM} = \frac{1}{21}\sum_{i=1}^{21} (N_i \times M_i) = 0.0826$$

So we have a equals to 184.5, b equals to 11.92 and r equals to 1.

A comparison between the fitting result and the theoretical calculation result is given in Table 7. It can be seen that the error of the first-order coefficient between the experimental test result and the theoretical calculation result does not exceed 2.2%. The correlation coefficient is 1, which verifies the high linearity relationship between M and N.

Moreover, the position error could be obtained by

$$\overline{\Delta N} = \frac{1}{20}\sum_{i=1}^{20} \Delta N_i = 0.2$$

$$\sigma_N = \frac{1}{20}\sum_{i=1}^{20} \left(\Delta N_i - \overline{\Delta N}\right) = 1.8997 \times 10^{-5}$$

So we got the angular position error of the focal plane adjustment mechanism is

$$3\sigma_N = 5.6990 \times 10^{-5}$$

It is 0.0034′ after unit conversion, verifying the high positioning accuracy of the drift angle compensation mechanism.

5. MTF analysis

As is introduced, drift angle may degrade the imaging quality of space cameras. Additionally, during process of drift angle compensation, yaw angle adjustment error, drift angle calculation error, mechanism positioning error and nonlinear motion error will all cause the image quality to drop.

5.1. Drift angle error analysis

Parameter errors will lead to errors of the results in the drift angle calculation process. However, the analytical formula of the

Table 8
Errors of the parameters for drift angle calculation.

Item	1	2	3	4	5	6	7	8	9
Parameters	i_0 (°)	F (mm)	H (km)	h (km)	γ_0 (°)	φ_0 (°)	θ_0 (°)	ψ_0 (°)	Ω (s^{-1})
Values	0.01	3	0.05	0.05	0.015	0.02	0.02	0.02	1×10^{-6}

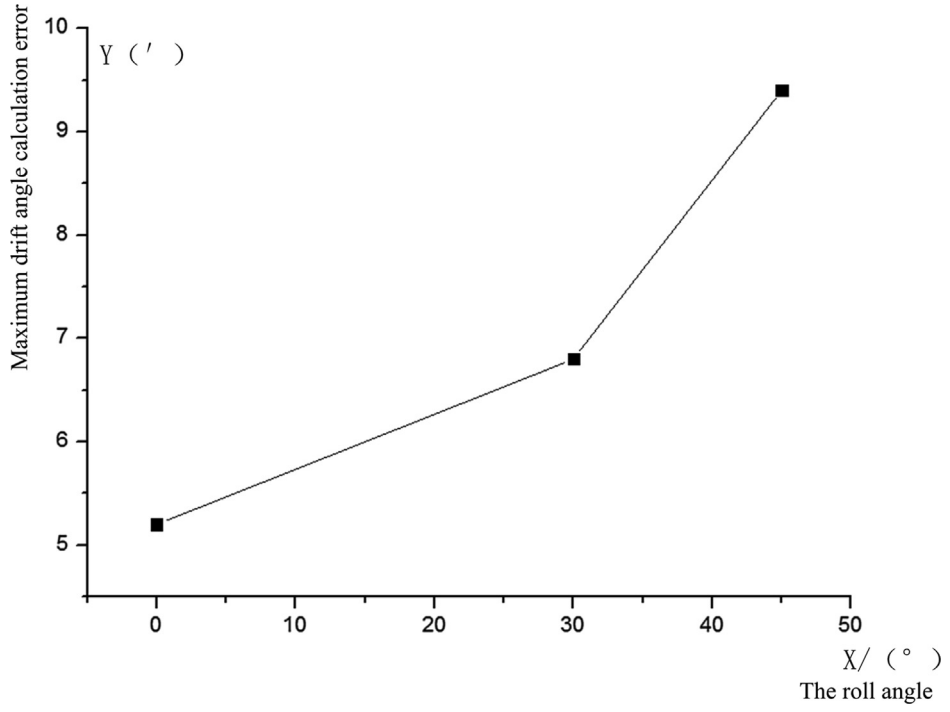

Fig. 15. Maximum drift angle calculation errors in cases of different roll angles.

Table 9
Error distribution of drift angle when roll angle is 45°.

Item	Error	Error nature	Limit error	Error distribution	Confidence factor	Standard deviation
1	Drift angle calculation error σ_1	Random error	±9.4′	Normal distribution	3	±3.13′
2	Focal plane mounting error in yaw direction σ_2	System error	±1′	Uniform distribution		±0.577′
3	Camera coordinate system mounting error relative to the star sensor coordinate system in yaw direction σ_3	System error	±1′	Uniform distribution		±0.577′
4	Distortional drift angle σ_4	Fixed system error	±0.7′		1	±0.7′
5	Yaw angle cumulative error σ_5	System error	±1.5′	Uniform distribution		±0.866′

Table 10
Drift angle for MTF calculation.

Parameter	Maximum drift angle β1	Drift angle error β2	Drift angle for yaw adjustment β3	Yaw adjustment error β4	Compensation of mechanism β5	Nonlinear error of mechanism β6	Positioning error of mechanism β7
Value	172.0'	10.75'	142.1'	1.2'	10.4'	0.06'	0.0034'
	β12 = β1 + β2 = 182.75′		\	\	\	\	\
	β14 = β1 + β2-β3 + β4- = 41.85′				\	\	\
	β17 = β1 + β2-β3 + β4-β5 + β6 + β7 = 31.5134′						

drift angle calculation is too complicated to solve. The parameters for calculation obey the Gaussian distribution, so sets of random numbers individually for each parameters obeying the Gaussian distribution were generated by a computer according to the limit deviations (3σ) and the expected values. The Monte Carlo method was used to estimate the error of the drift angle calculation result. Errors of the parameters are shown in Table 8.

So the drift angle calculation errors under conditions of different roll angles were obtained, which are shown in Fig. 15. It can be seen that the maximum drift angle calculation error increases as the roll angle increases, and reaches a maximum value of 9.4′ when the roll angle is 45°.

Additionally, errors from the satellite platform, optical system and other factors also contribute the drift angle error. The error distribution is shown in Table 9.

So the drift angle error after synthesis is

$$\sigma = \pm\left(3\sqrt{\sigma_1^2+\sigma_2^2+\sigma_3^2+\sigma_5^2}+\sigma_4\right) = 10.75'$$

5.2. MTF analysis

Through the above calculation and analysis, it can be seen that under condition that the rolling angle is 45°, the difference of the drift angles on the focal plane and the drift angle calculation error reach the maximum values. In this condition, the drift angle calculation error is 10.75′ and the average drift angle for yaw adjustment is −142.1′. The yaw adjustment error is 1.2′, the maximum drift angle difference between positions of the focal plane is 29.9′ and it is reduced to 19.5′ after mechanism adjustment. The linear error of the mechanism adjustment is 0.06′, and the mechanism positioning error is about 0.0034′. All these factors may cause MTF drop. After the average yaw angle is compensated by yaw adjustment, the transfer angle function is obtained by using the calculation formula (14) [1]

$$MTF = \frac{\sin\left(\frac{\pi}{2}\times\frac{f_C}{f_N}\times N\times\tan\beta\right)}{\frac{\pi}{2}\times\frac{f_C}{f_N}\times N\times\tan\beta} \tag{14}$$

In the equation, f_C and f_N are characteristic frequencies and they are equal to each other. N is the TDICCD level which equals to 32. β represents the comprehensive drift angle. After substitution of the data in Table 10 for calculation, MTF results corresponding to β12, β14 and β17 were obtained. It can be seen that the drift angle is 182.75′ without any compensation and the MTF is 0.1683(MTF reduced by 83.17%). After yaw adjustment, the drift angle is reduced to 41.85′, and the MTF turns to 0.9387(MTF reduced by 6.13%). After compensation of mechanism, the drift angle becomes 31.5134′, and the MTF increase to 0.9650(MTF reduced by 3.50%). The nonlinear error of the mechanism only contributes 1.9‰ to the drift angle and is small enough to be neglected. Additionally, the drop ratio of the MTF does not exceed 5%, which satisfies the imaging quality requirement of TDICCD.

6. Conclusions

This work proposed the use of satellite yaw-angle adjustment and camera focal plane adjustment combined to achieve drift angle compensation for high-resolution, wide-range remote sensing cameras. Drift angle distribution was obtained by calculation and the angle for yaw angle adjustment and further compensation by mechanism were calculated. A focal plane adjustment mechanism and the motion linearity of it were designed. A theoretical calculation model of the mechanism motion was established, analyzed and verified by laboratory tests. It can be seen from the results that the comparison error of the linearity coefficient and non-linearity residual between the test results and theoretical calculation results is less than 2.2%, which verifies the high degree of coincidence. The non-linearity residuals of both test results and theoretical calculation results are less than 0.03%, which verifies the high compensation linearity required to meet the requirement of high-precision adjustment. Finally, MTF analysis was conducted and the result showed: 1. As the MTF reduction decreases by 42.9% after mechanism compensation, compensation by focal plane adjustment can effectively eliminate the residual of drift angle after yaw adjustment. 2. After compensation of drift angle combined by yaw and mechanism adjustment, the MTF drop ratio is 3.5%, which satisfies the imaging quality requirement of TDICCD. 3. The nonlinear error of the mechanism only contributes 1.9‰ to the drift angle, so it effects little on the MTF. So we can see that through this method introduced in the paper, compensation by a high linearity focal plane adjustment can effectively eliminate the residual of drift angle after yaw adjustment. Which could help satisfy the imaging quality requirement of TDICCD.

CRediT authorship contribution statement

Wenyan Li: Conceptualization. **Chunhui Hu:** Data curation. **Lei Zhang:** Formal analysis. **Changxiang Yan:** Funding acquisition.

Declaration of Competing Interest

The authors declare that they have no known competing financial interests or personal relationships that could have appeared to influence the work reported in this paper.

Acknowledgment

We would like to thank Editage (www.editage.com) for English language editing.

References

[1] J.Q. Wang, System Design of Optical Instrument, Academe of Changchun Institute of Optics and Mechanics, Changchun, 2003 (in Chinese).
[2] Y. Sun et al., Drift angle distribution and image quality decreasing of solar synchronizing elliptic orbit, Infrared Laser Eng. 42 (03) (2013) 767–773 (in Chinese).
[3] Y.N. Wu et al., Image motion compensation and MTF analyse of long array TDICCD space camera, Electron. Measure. Technol. 37 (10) (2014), 71-75+80 (in Chinese).
[4] T. Yu et al., Batch-type real-time adjustment for drift angle of space camera, Opt. Precis. Eng. 17 (08) (2009) 1908–1914 (in Chinese).
[5] S.H. Ren et al., Analysis of drift adjustment by a space optical camera platform, J. Spacecraft TT&C Technol. 36 (04) (2017) 281–286 (in Chinese).
[6] M. Huang et al., Analysis on image motion velocity and drift angle for agile satellite, Spacecraft Eng. 24(03) (2015) 34–39 (in Chinese).
[7] K. Xu et al., Design of motion adjusting system for space camera based on ultrasonic motor, Space Explor. Technol. Appl. Proc. SPIE 8196 (2011).
[8] H. Bao et al., Design of draft adjusting mechanism for space optical camera, Opto-Electron. Eng. 39 (6) (2012) 22–27 (in Chinese).
[9] S. Gu et al., Design of motion compensation mechanism of satellite remote sensing camera, Space Explor. Technol. Appl., Proc. SPIE 8196 (2011).
[10] H.S. Yang et al., Kinematic formula fitting of drift adjusting mechanism for space camera, Opt. Precis. Eng. 22 (12) (2014) 3342–3347 (in Chinese).
[11] Y.C. Li et al., Image motion velocity field of off-axis TMA space camera with large field of view, Infrared Laser Eng. 45 (05) (2016) 174–181 (in Chinese).
[12] X.K. Yuan, Calculation and compensation for the deviant angle of satellite borne TDI-CCD push scan camera, Aerosp. Shanghai. 06 (2006) 10–13 (in Chinese).
[13] X.K. Yuan, Computation model of image motion velocity for space borne cameras, Aerosp. Shanghai 03 (2008) 1–5 (in Chinese).
[14] Y. Li et al., Image motion compensation of off-axis TMA three-line array aerospace mapping cameras, J. Harbin Inst. Technol. 23 (6) (2016) 80–89 (in Chinese).
[15] C. Yan, J. Wang, Method of coordinate transformation for IM&IMC calculation in aerospace camera system, Opt. Precis. Eng. 8 (3) (2000) 203–207 (in Chinese).
[16] P.L. Lu et al., Image motion velocity field model of space camera with large field and analysis on three-axis attitude stability of satellite, Opt. Precis. Eng. 24 (09) (2016) 2173–2182 (in Chinese).
[17] F.N. Long, W. Zhang, J.F. Liu, Effect of satellite attitude control accuracy on TDI CCD cameras, J. Harbin Inst. Technol. 03 (2002) 382–384 (in Chinese).
[18] Y. Hu et al., Image motion catching calculation and imaging validation of TDI CCD camera on elliptical orbit, Opt. Precis. Eng. 22 (08) (2014) 2274–2284 (in Chinese).
[19] C. Fan, Y.C. Li, H.W. Yi, Analysis of drift angle on space camera, Infrared Laser Eng. 35 (2006) 216–220 (in Chinese).
[20] C. Fan, Y.T. Liang, W. Yi, Study on influence of drift angle on the space camera, Electron. Opt. Control 15 (11) (2008) 76–79 (in Chinese).

Wenyan Li is an assistant researcher of Changchun Institute of Optics, Fine Mechanics and Physics, Chinese Academy of Sciences, Ph.D. candidate of University of Chinese Academy of Sciences researching on design of space telescope.

Chunhui Hu is an assistant researcher of Changchun Institute of Optics, Fine Mechanics and Physics, Chinese Academy of Sciences, doctor of University of Chinese Academy of Sciences researching on design of space telescope.

Lei Zhang is a professor of Changchun Institute of Optics, Fine Mechanics and Physics and a doctoral tutor of Chinese Academy of Sciences, whose researches on development and theoretical research of space optics.

Changxiang Yan is a professor of Changchun Institute of Optics, Fine Mechanics and Physics and a doctoral tutor of Chinese Academy of Sciences, whose researches on development and theoretical research of space optics.